Supplement of Atmos. Chem. Phys., 22, 12367–12386, 2022
https://doi.org/10.5194/acp-22-12367-2022-supplement

Atmospheric Chemistry and Physics
Open Access
EGU

Supplement of

Evaluating the contribution of the unexplored photochemistry of aldehydes on the tropospheric levels of molecular hydrogen (H_2)

Maria Paula Pérez-Peña et al.

Correspondence to: Jenny A. Fisher (jennyf@uow.edu.au) and Maria Paula Pérez-Peña (m.perez_pena@unsw.edu.au)

1 Mixing ratios results from the box modelling

The mixing ratios in the baseline simulations provide context for our box modelling results. Select modelled species from the baseline simulations for London, Cape Verde and Borneo are shown in Figures S1-S3 respectively. The baseline mixing ratio of H_2 increased continuously from its initial value of 530 ppbv to 639.97 ppbv at London and 533.96 ppbv at Borneo. At Cape Verde, the mixing ratio of H_2 decreased during the simulated period to 517.23 ppbv. These changes are equivalent to an increase in H_2 of ∼17% over 12 days for London, an increase of ∼1% over 6 days for Borneo, and a decrease of ∼2% over 12 days for Cape Verde. These final H_2 mixing ratios are not representative of the actual values over the selected locations particularly because of the lack other relevant physical processes such as emissions, transport and uptake by soil.

For the London and Borneo simulations, the H_2 increase over time in the baseline run was effectively caused by the photolysis of formaldehyde and glyoxal (the only H_2 sources in this simulation). The decrease in modelled H_2 at Cape Verde was a result of imbalances in the chemical sources and sinks in this regime. For the Cape Verde simulation, neither formaldehyde nor glyoxal had available measurement constraints (see Table Table 1 in the manuscript); however, both were produced chemically, with formaldehyde production from the degradation of methane, ethene, propene, toluene and benzene and glyoxal production from ethene and toluene precursors (Stavrakou et al., 2009). These five precursor species were all constrained in the Cape Verde simulations (see Table Table 1, footnote b). Figure S2 shows the time series of selected species modelled for Cape Verde, including formaldehyde, which had an average modelled value of ∼800 pptv (∼2×10^{10} molecules cm^{-3}). For comparison, Whalley et al., 2010 reported an average noon value of 328 pptv for their MCM simulations at Cape Verde during May-June 2007 (note that they do not report values for glyoxal). Considering that our modelled formaldehyde mixing ratios were higher than those reported previously by Whalley et al., 2010, and because of the formaldehyde and glyoxal lifetimes of a few hours, we conclude that our simulations included sufficient precursor concentrations and therefore that the decrease in H_2 in the baseline Cape Verde simulation implies that the available H_2 was consumed by OH more rapidly than it could be produced by formaldehyde and glyoxal, yielding an effective loss over the 12 days modelled.

2 Dry deposition velocity calculation in Yashiro et al., 2011

The dry deposition velocity on the surface of the inactive layer was calculated by Yashiro et al., 2011 as:

$$Vd = \frac{1}{\frac{\delta}{Ds\theta_a} + \sqrt{\frac{1}{Dsk\theta_a}}} \tag{1}$$

where θ_a is volume of gas per unit volume of soil (air filling porosity) [$m^3\ m^{-3}$], Ds is the diffusivity in soil, k is the biological uptake rate [s^{-1}] dependent on soil temperature and soil moisture (see Yashiro et al., 2011 equations 13 to 16). For the diffusivity

$$Ds = Da\frac{\theta_a^{3.1}}{\theta_{sat}^2} \tag{2}$$

where Da is the molecular diffusion coefficient with a value for H_2 of 0.611 $cm^2\ s^{-1}$ and θ_{sat} is the maximum aerial or liquid water volume per unit volume of soil (total porosity).

The parameterisation to derive the dry deposition velocity for H_2 used by Yashiro et al., 2011 implements the same variables as that used by Ehhalt and Rohrer, 2013. The Ehhalt and Rohrer, 2013 parameterisation, applied recently by Paulot et al., 2021, differs from the one by Yashiro et al., 2011 in that the latter considers the diffusivity in the soil to be uniform from the soil surface to a sufficient depth (because the diffusivity is within the first layer of the parent land model), while Ehhalt and Rohrer, 2013 use two different soil diffusivities. Further, the biological activity (uptake rate k), soil moisture and soil temperature dependencies are also different between Yashiro et al., 2011 and Ehhalt and Rohrer, 2013. Yashiro et al., 2011 follow the variation of the biological activity from Smith-Downey et al., 2006, while Ehhalt and Rohrer, 2013 rely on the dependencies from the reanalysis performed by Ehhalt and Rohrer, 2011. Also, the thickness of the inactive layer used by Yashiro et al., 2011 is considered to be uniform (with a value of 0.7 cm) while Ehhalt and Rohrer, 2013 provide values that are a function of the average volumetric soil water content. Even though both models start from equation 3 (where Fs is the flux and C is the mass concentration of H_2) to derive the dry deposition velocity as a function of the H_2 flux and diffusivities, the two models differ when the thickness of the inactive layer $\delta = 0$ as a consequence of the difference in the definition of the flux.

$$Vd = \frac{Fs}{\rho C} \tag{3}$$

Ehhalt and Rohrer, 2013 used equation 4, where Ms corresponds to the H_2 mixing ratio in the soil air.

$$Fs = -Ds\rho\frac{\delta Ms}{\delta z} \tag{4}$$

On the other hand, Yashiro et al., 2011 used equation 5

$$Fs = -Ds\rho\theta_a\frac{\delta Ms}{\delta z} \tag{5}$$

This equation originated from equations (2), (3) and (4) in Yonemura et al., 2000. The version used by Yashiro et al., 2011 (equation 5) means that the gradient of the gas concentration between the two layers is determined not only by the mixing ratio, but also by the air-filled porosity.

References

Yonemura, S., Kawashima, S., & Tsuruta, H. (2000). Carbon monoxide, hydrogen, and methane uptake by soils in a temperate arable field and a forest. *Journal of Geophysical Research Atmospheres*, *105*(D11), 14347–14362. https://doi.org/10.1029/1999JD901156

Smith-Downey, N. V., Randerson, J. T., & Eiler, J. M. (2006). Temperature and moisture dependence of soil H2 uptake measured in the laboratory. *Geophysical Research Letters*, *33*(14), 1–5. https://doi.org/10.1029/2006GL026749

Fu, T. M., Jacob, D. J., Wittrock, F., Burrows, J. P., Vrekoussis, M., & Henze, D. K. (2008). Global budgets of atmospheric glyoxal and methylglyoxal, and implications for formation of secondary organic aerosols. *Journal of Geophysical Research Atmospheres*, *113*(15). https://doi.org/10.1029/2007JD009505

Stavrakou, T., Muller, J. F., De Smedt, I., Van Roozendael, M., Kanakidou, M., Vrekoussis, M., Wittrock, F., Richter, A., & Burrows, J. P. (2009). The continental source of glyoxal estimated by the synergistic use of spaceborne measurements and inverse modelling. *Atmospheric Chemistry and Physics*, *9*(21), 8431–8446. https://doi.org/10.5194/acp-9-8431-2009

Whalley, L. K., Furneaux, K. L., Goddard, A., Lee, J. D., Mahajan, A., Oetjen, H., Read, K. A., Kaaden, N., Carpenter, L. J., Lewis, A. C., C. Plane, J. M., Saltzman, E. S., Wiedensohler, A., & Heard, D. E. (2010). The chemistry of OH and HO2 radicals in the boundary layer over the tropical Atlantic Ocean. *Atmospheric Chemistry and Physics*, *10*(4), 1555–1576. https://doi.org/10.5194/acp-10-1555-2010

Ehhalt, D. H., & Rohrer, F. (2011). The dependence of soil H2 uptake on temperature and moisture: A reanalysis of laboratory data. *Tellus, Series B: Chemical and Physical Meteorology*, *63*(5), 1040–1051. https://doi.org/10.1111/j.1600-0889.2011.00581.x

Yashiro, H., Sudo, K., Yonemura, S., & Takigawa, M. (2011). The impact of soil uptake on the global distribution of molecular hydrogen: Chemical transport model simulation. *Atmospheric Chemistry and Physics*, *11*(13), 6701–6719. https://doi.org/10.5194/acp-11-6701-2011

Ehhalt, D. H., & Rohrer, F. (2013). Deposition velocity of H2: A new algorithm for its dependence on soil moisture and temperature. *Tellus, Series B: Chemical and Physical Meteorology*, *65*(1). https://doi.org/10.3402/tellusb.v65i0.19904

Krummel, P. B., Langenfelds, R. L., & Loh, Z. (2021a). Atmospheric CO at Alert by Commonwealth Scientific and Industrial Research Organisation, dataset published as CO_ALT_surface-flask_CSIRO_data1 at WDCGG, ver. 2021-07-05-0440. https://doi.org/ttps://doi.org/10.50849/WDCGG{_}0016-4001-3001-01-02-9999

Krummel, P. B., Langenfelds, R. L., & Loh, Z. (2021b). Atmospheric CO at Cape Ferguson by Commonwealth Scientific and Industrial Research Organisation, dataset published as CO_CFA_surface-flask_CSIRO_data1 at WDCGG, ver. 2021-07-05-0440. https://doi.org/https://doi.org/10.50849/WDCGG{_}0016-5010-3001-01-02-9999

Krummel, P. B., Langenfelds, R. L., & Loh, Z. (2021c). Atmospheric CO at Cape Grim by Commonwealth Scientific and Industrial Research Organisation, dataset published as CO_CGO_surface-flask_CSIRO_data1 at WDCGG, ver. 2021-07-05-0440. https://doi.org/https://doi.org/10.50849/WDCGG{_}0016-5011-3001-01-02-9999

Krummel, P. B., Langenfelds, R. L., & Loh, Z. (2021d). Atmospheric CO at Casey by Commonwealth Scientific and Industrial Research Organisation, dataset published as CO_CYA_surface-flask_CSIRO_data1 at WDCGG, ver. 2021-07-05-0440. https://doi.org/https://doi.org/10.50849/WDCGG{_}0016-7004-3001-01-02-9999

Krummel, P. B., Langenfelds, R. L., & Loh, Z. (2021e). Atmospheric CO at Macquarie Island by Commonwealth Scientific and Industrial Research Organisation, dataset published as CO_MQA_surface-flask_CSIRO_data1 at WDCGG, ver. 2021-07-05-0440. https://doi.org/https://doi.org/10.50849/WDCGG{_}0016-5015-3001-01-02-9999

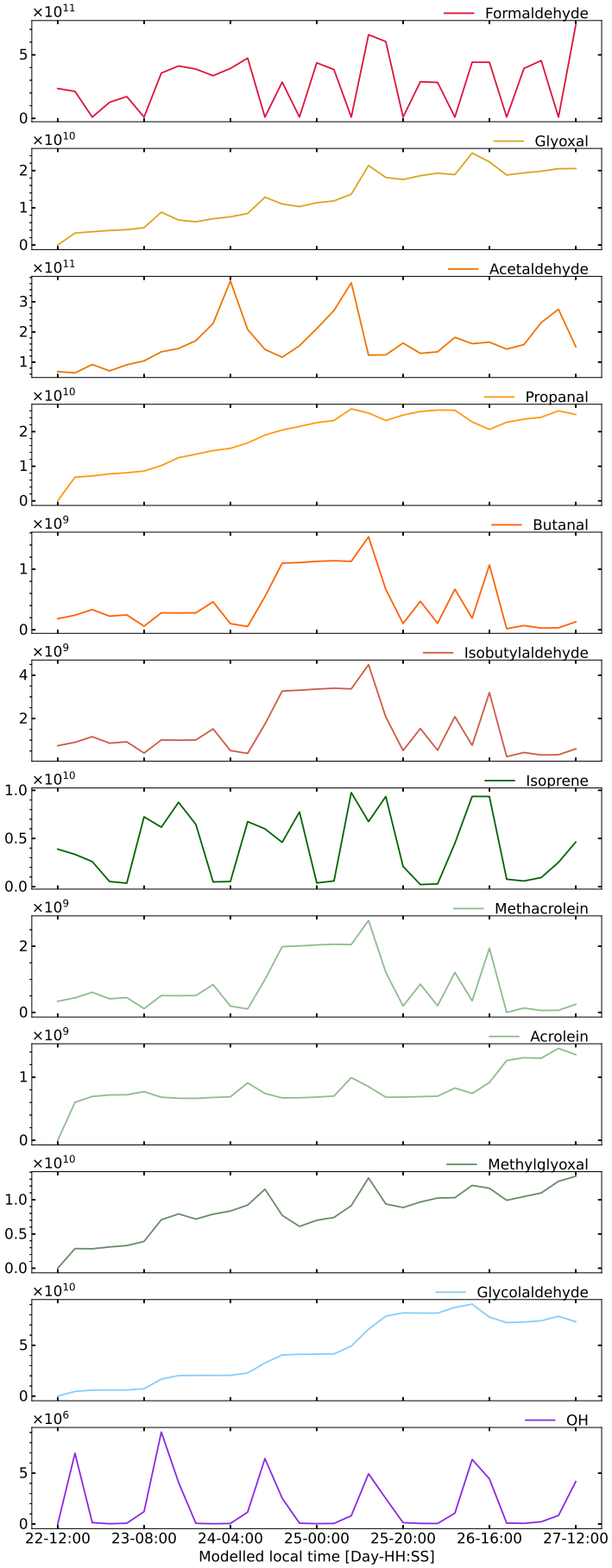

Figure S1: Time series for selected modelled species in molecules cm^{-3} from the baseline box model simulation in London starting at noon on the 22^{nd} of July 2012.

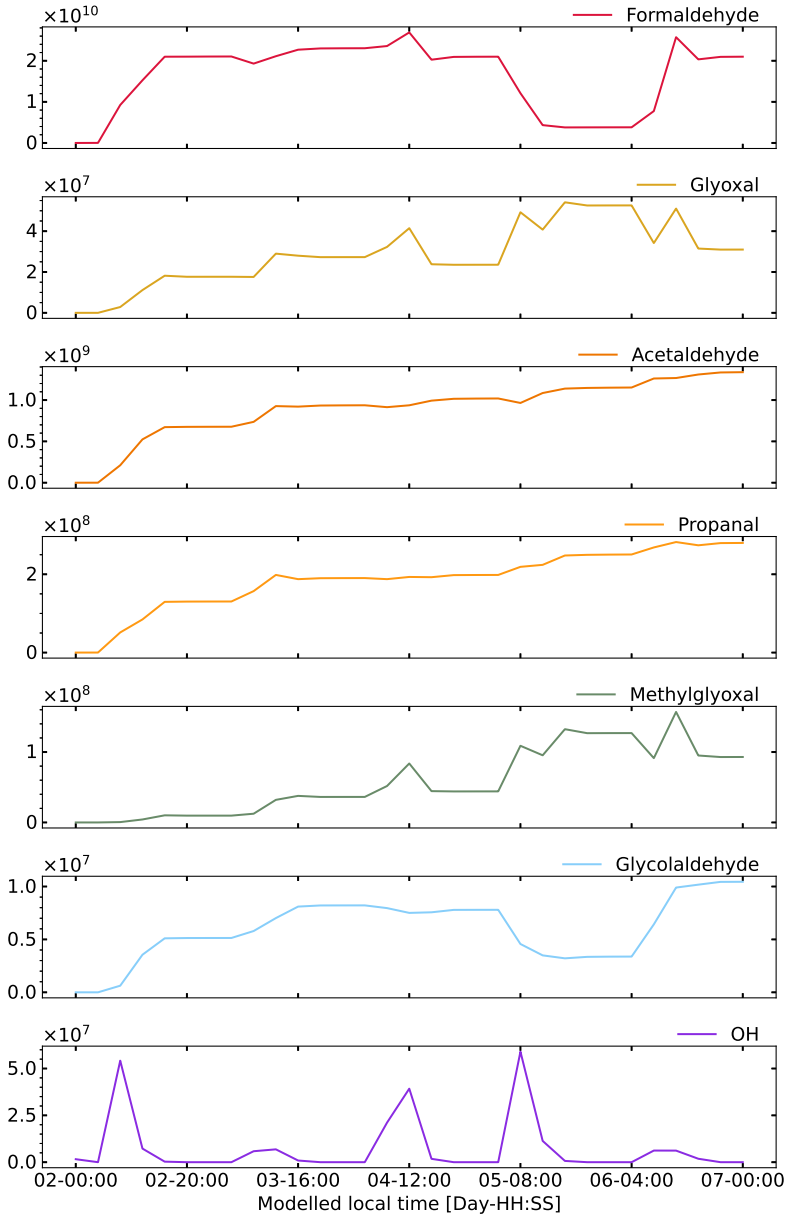

Figure S2: Time series for selected modelled species in molecules cm^{-3} from the baseline box model simulation in Cape Verde starting at midnight on the 2^{nd} of January 2015.

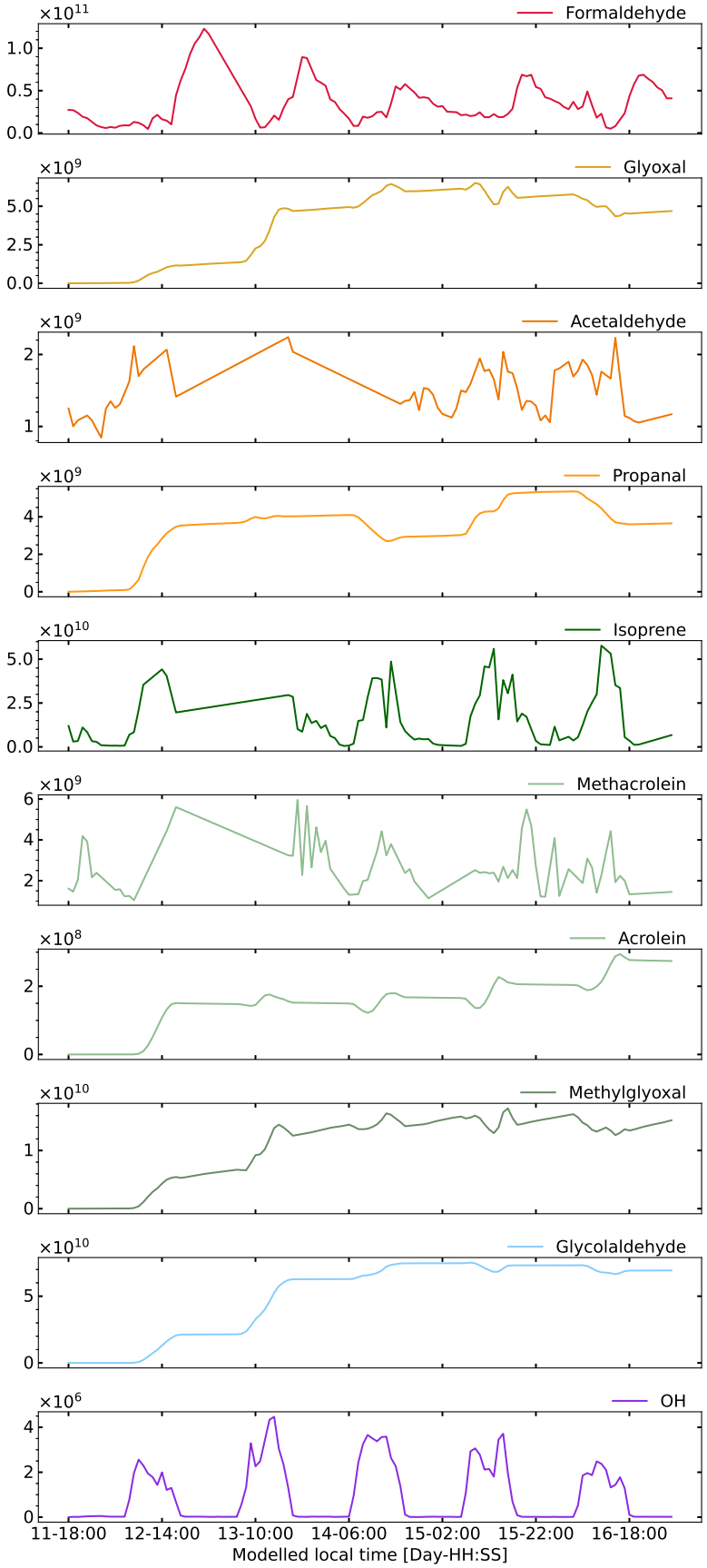

Figure S3: Time series for selected modelled species in molecules cm^{-3} from the baseline box model simulation in Borneo starting at 18:00 on the 11^{th} of July 2008.

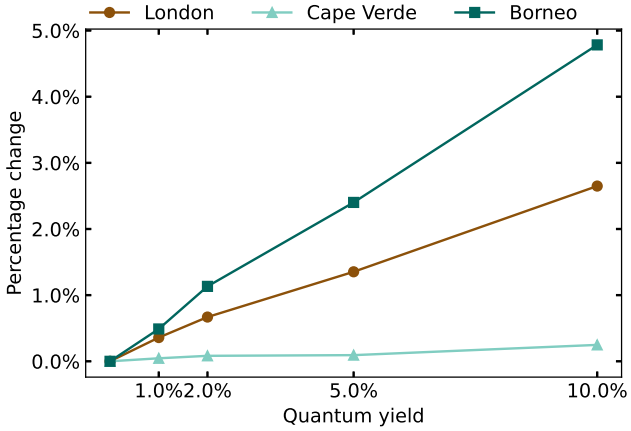

Figure S4: Percentage change in the total rate of production of H_2 from aldehydes for varying quantum yields calculated relative to the baseline simulation at the three tested sites for 1 modelled day (local time)

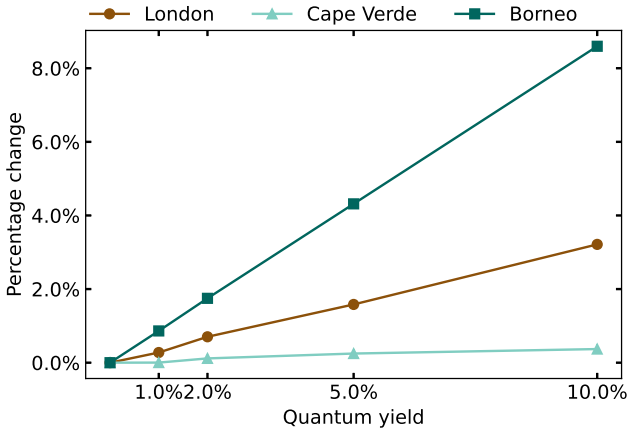

Figure S5: Percentage change in the total rate of production of H_2 from aldehydes for varying quantum yields at the three tested sites for 5 modelled days (local time)

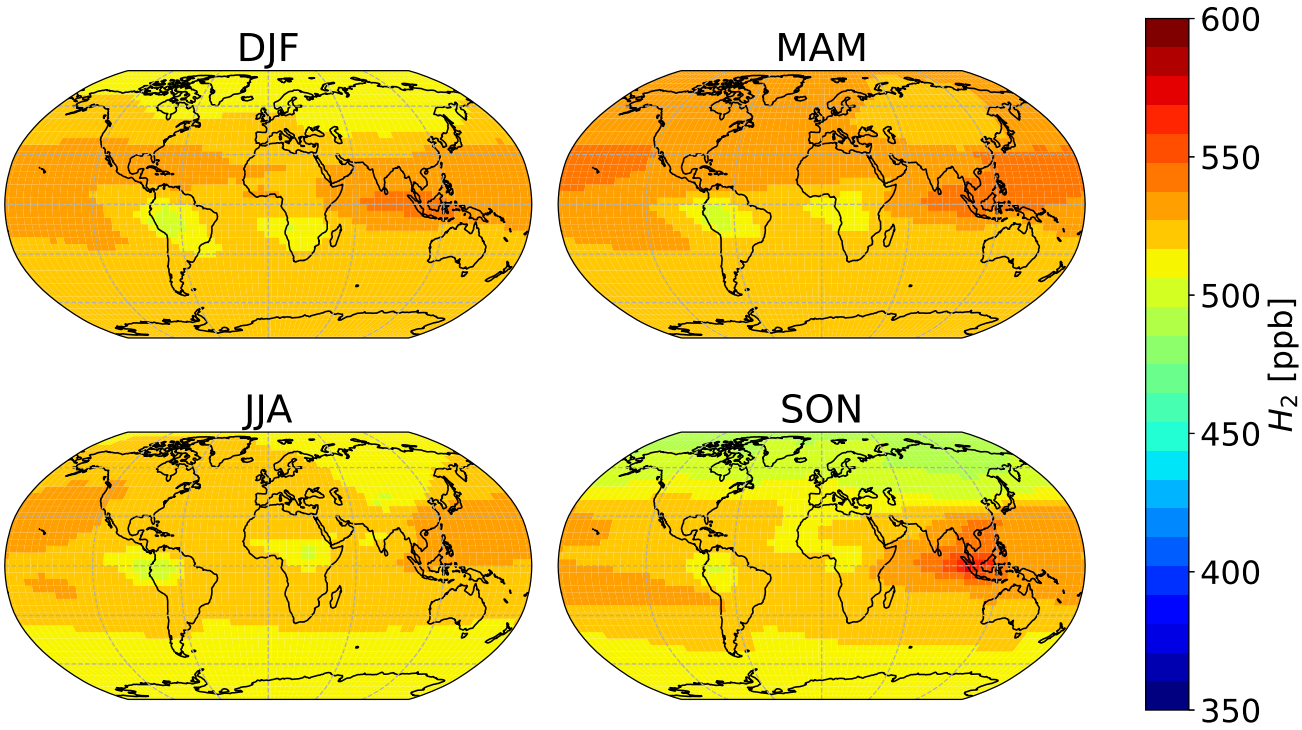

Figure S6: Average modelled mixing rations of H_2 per season estimated with GEOS-Chem at 500 hPa for 2015 and 2016.

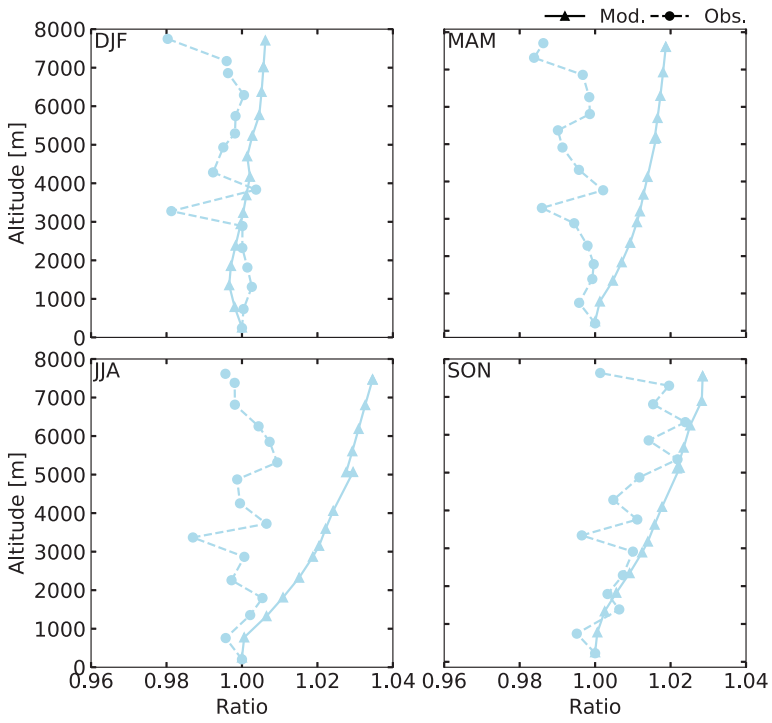

Figure S7: Seasonal comparison between average modelled (triangles) and average observed (circles) H_2 estimated ratios at different heights with respect to the surface layer. Modelled averaged values are from 2015 and 2016. Observations averaged values are those from the Aircraft (AIA) flask sampling data from Krummel et al., 2021r

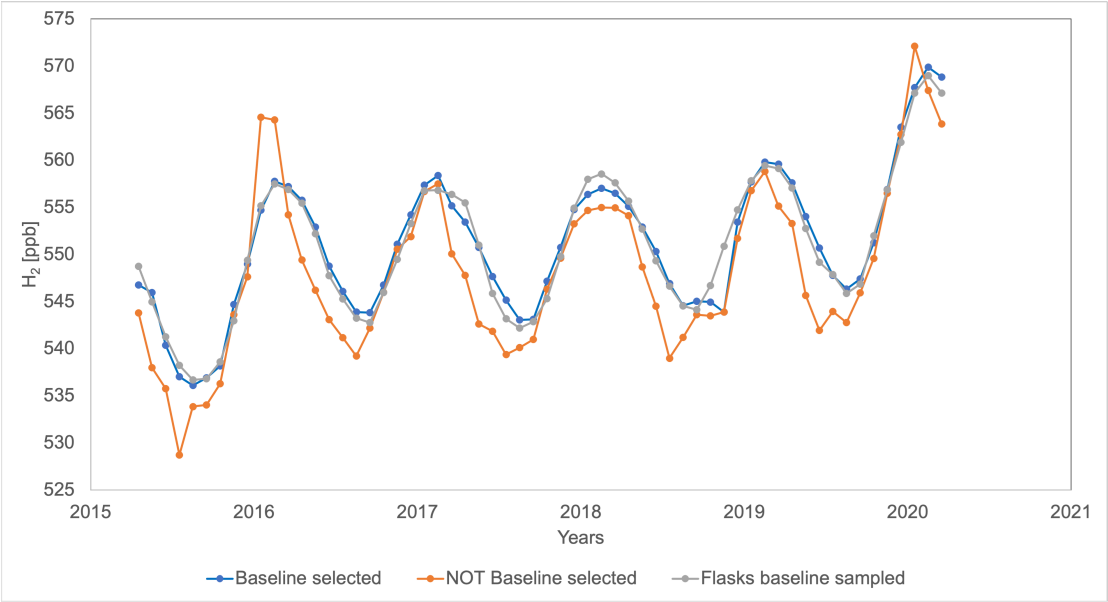

Figure S8: Comparison between baseline-selected in-situ data, baseline-sampled data measured with a PDD detector (blue and orange line) and flask baseline sampled by CSIRO at Cape Grim from April 2015.

Krummel, P. B., Langenfelds, R. L., & Loh, Z. (2021f). Atmospheric CO at Mauna Loa by Commonwealth Scientific and Industrial Research Organisation, dataset published as CO_MLO_surface-flask_CSIRO_data1 at WDCGG, ver. 2021-07-05-0440. https://doi.org/https://doi.org/10.50849/WDCGG{_}0016-5002-3001-01-02-9999

Krummel, P. B., Langenfelds, R. L., & Loh, Z. (2021g). Atmospheric CO at Mawson by Commonwealth Scientific and Industrial Research Organisation, dataset published as CO_MAA_surface-flask_CSIRO_data1 at WDCGG, ver. 2021-07-05-0440. https://doi.org/https://doi.org/10.50849/WDCGG{_}0016-7005-3001-01-02-9999

Krummel, P. B., Langenfelds, R. L., & Loh, Z. (2021h). Atmospheric CO at South Pole by Commonwealth Scientific and Industrial Research Organisation, dataset published as CO_SPO_surface-flask_CSIRO_data1 at WDCGG, ver. 2021-07-05-0440. https://doi.org/https://doi.org/10.50849/WDCGG{_}0016-7011-3001-01-02-9999

Krummel, P. B., Langenfelds, R. L., & Loh, Z. (2021i). Atmospheric CO by Aircraft (over Bass Strait and Cape Grim), Commonwealth Scientific and Industrial Research Organisation, dataset published as CO_AIA_aircraft-flask_CSIRO_data1 at WDCGG, ver. 2021-07-05-0440. https://doi.org/https://doi.org/10.50849/WDCGG{_}0016-8003-3001-05-02-9999{\}

Krummel, P. B., Langenfelds, R. L., & Loh, Z. (2021j). Atmospheric H2 at Alert by Commonwealth Scientific and Industrial Research Organisation, dataset published as H2_ALT_surface-flask_CSIRO_data1 at WDCGG, ver. 2021-07-05-0440. https://doi.org/https://doi.org/10.50849/WDCGG{_}0016-4001-4001-01-02-9999

Krummel, P. B., Langenfelds, R. L., & Loh, Z. (2021k). Atmospheric H2 at Cape Ferguson by Commonwealth Scientific and Industrial Research Organisation, dataset published as H2_CFA_surface-flask_CSIRO_data1 at WDCGG, ver. 2021-07-05-0440. https://doi.org/https://doi.org/10.50849/WDCGG{_}0016-5010-4001-01-02-9999

Krummel, P. B., Langenfelds, R. L., & Loh, Z. (2021l). Atmospheric H2 at Cape Grim by Commonwealth Scientific and Industrial Research Organisation, dataset published as H2_CGO_surface-flask_CSIRO_data1 at WDCGG, ver. 2021-07-05-0440. https://doi.org/https://doi.org/10.50849/WDCGG{_}0016-5011-4001-01-02-9999

Krummel, P. B., Langenfelds, R. L., & Loh, Z. (2021m). Atmospheric H2 at Casey by Commonwealth Scientific and Industrial Research Organisation, dataset published as H2_CYA_surface-flask_CSIRO_data1 at WDCGG, ver. 2021-07-05-0440. https://doi.org/https://doi.org/10.50849/WDCGG{_}0016-7004-4001-01-02-9999

Krummel, P. B., Langenfelds, R. L., & Loh, Z. (2021n). Atmospheric H2 at Macquarie Island by Commonwealth Scientific and Industrial Research Organisation, dataset published as H2_MQA_surface-flask_CSIRO_data1 at WDCGG, ver. 2021-07-05-0440. https://doi.org/https://doi.org/10.50849/WDCGG{_}0016-5015-4001-01-02-9999

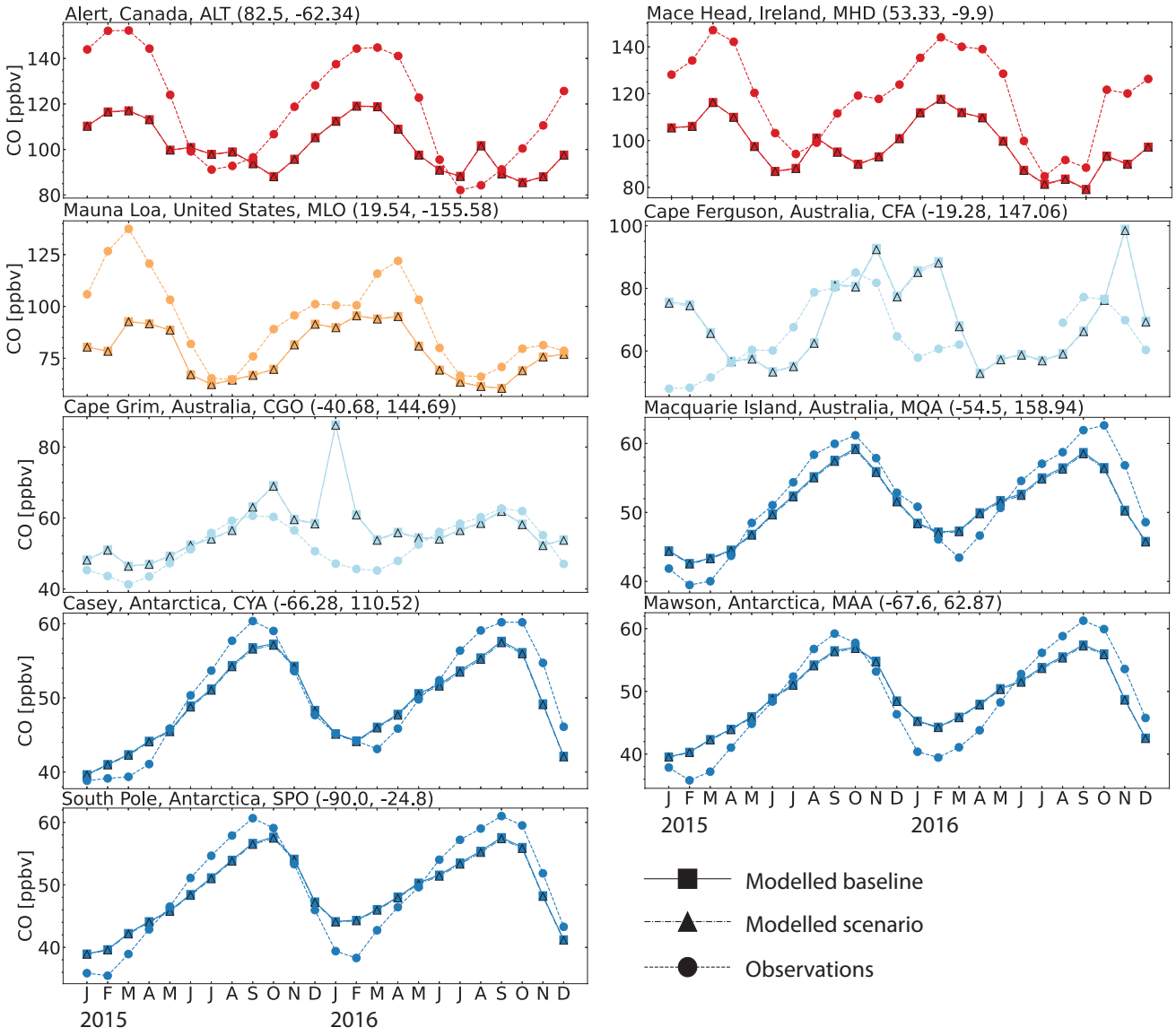

Figure S9: Seasonal cycle comparisons of CO at five sites from the CSIRO dataset (Krummel et al., 2021a, 2021b, 2021c, 2021d, 2021e, 2021f, 2021g, 2021h, 2021i) reported Flask Data for 2015 and 2016, the dash line with circle markers corresponds to observed values and the continuous line with triangle markers corresponds to modelled values in GEOS-Chem.

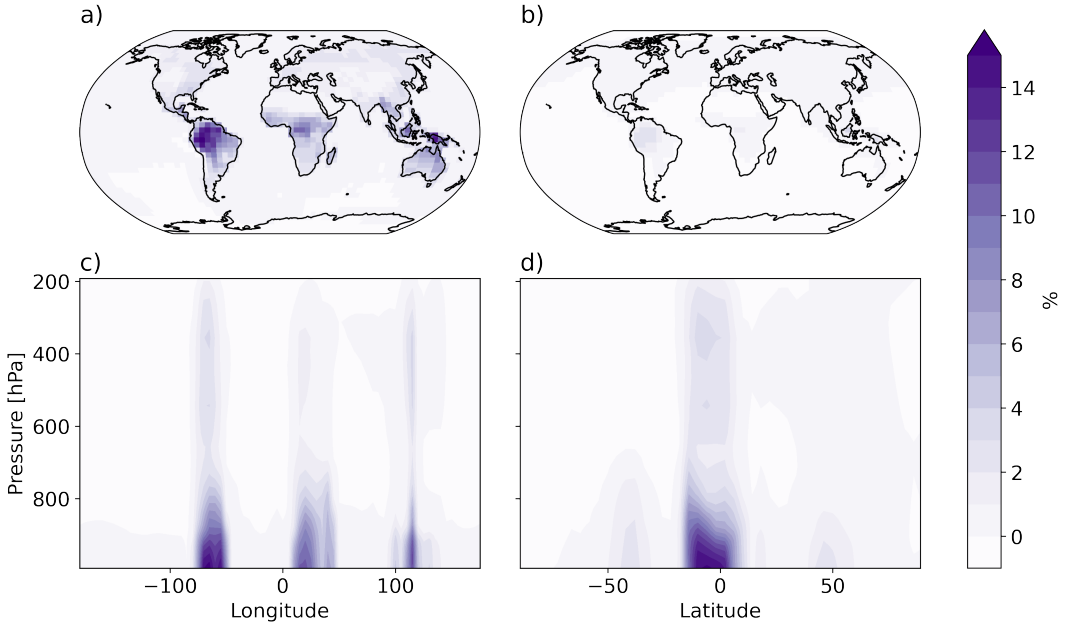

Figure S10: Percentage difference on the chemical production of H_2 between the 1% production of H_2 scenario and the baseline for a year a) At the surface level, b) At 500 hPa, c) Longitude section at 2 N and d) Latitude section at -70 W

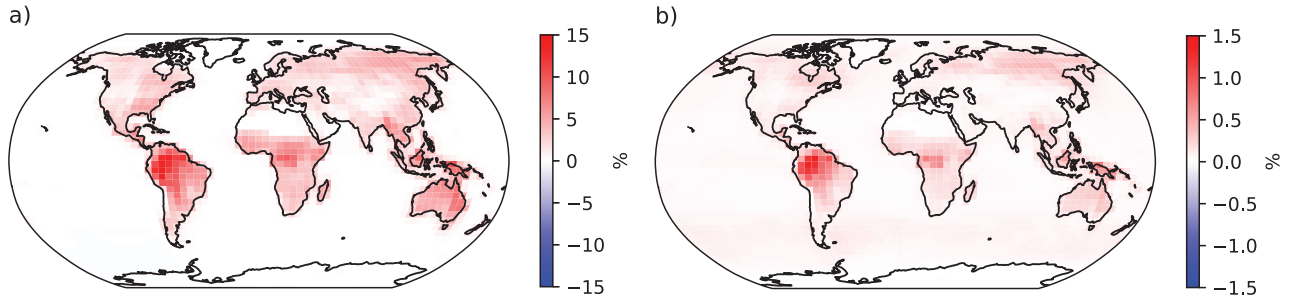

Figure S11: Percentage difference on the chemical production of H_2 between the 1% production of H_2 scenario and the baseline for a year at the surface layer from the photolysis of a) methylglyoxal b) acetaldehyde, HPALD, glycolaldehyde, methacrolein, lumped aldehydes with more than 3 carbon atoms RCHO (integrated)

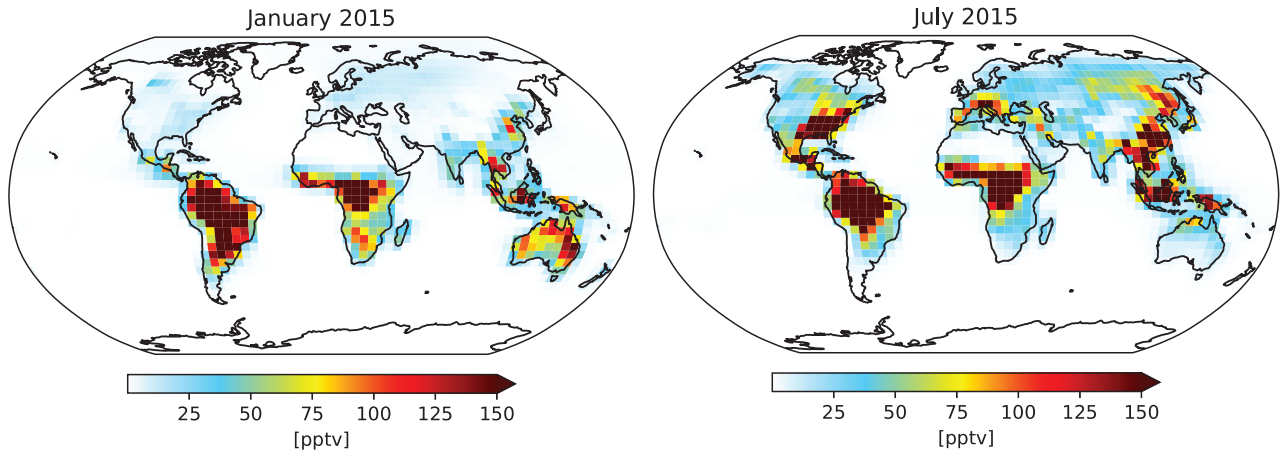

Figure S12: Simulated mixing ratios of methylglyoxal at the surface layer for January and July 2015. The modelled magnitudes of methylglyoxal in our GEOS-Chem simulation are comparable to those shown by Fu et al., 2008 in their Figure 2b.

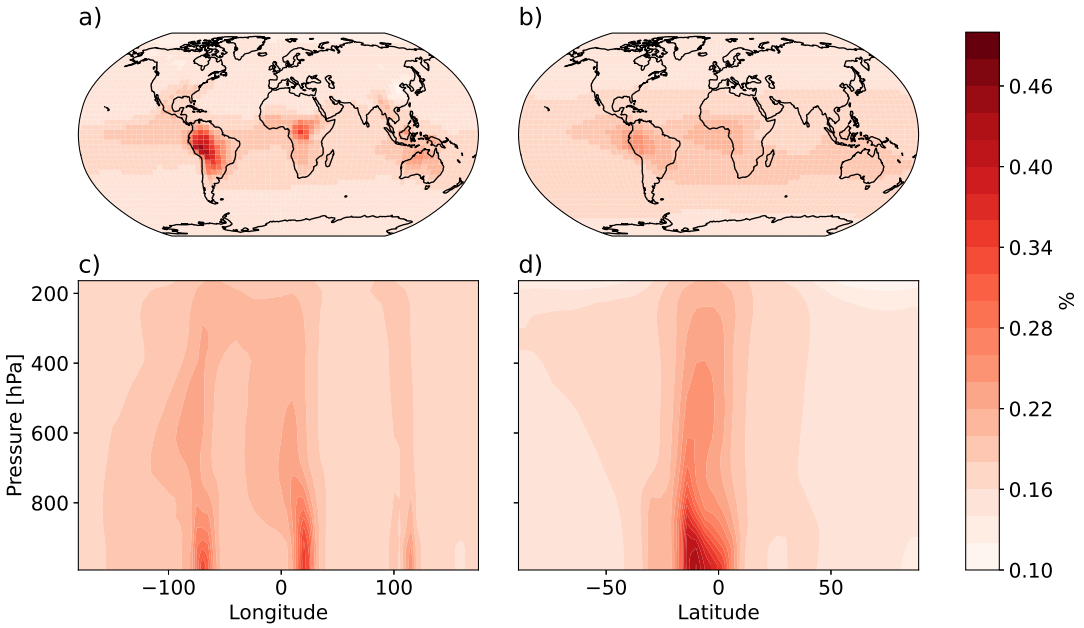

Figure S13: Percentage difference on the modelled mixing ratios of H_2 between the 1% production of H_2 scenario and the baseline for a year a) At the surface level, b) At 500 hPa, c) Longitude section at 2deg N and d) Latitude section at -70deg W

Krummel, P. B., Langenfelds, R. L., & Loh, Z. (2021o). Atmospheric H2 at Mauna Loa by Commonwealth Scientific and Industrial Research Organisation, dataset published as H2_MLO_surface-flask_CSIRO_data1 at WDCGG, ver. 2021-07-05-0440. https://doi.org/https://doi.org/10.50849/WDCGG{_}0016-5002-4001-01-02-9999,

Krummel, P. B., Langenfelds, R. L., & Loh, Z. (2021p). Atmospheric H2 at Mawson by Commonwealth Scientific and Industrial Research Organisation, dataset published as H2_MAA_surface-flask_CSIRO_data1 at WDCGG, ver. 2021-07-05-0440. https://doi.org/https://doi.org/10.50849/WDCGG{_}0016-7005-4001-01-02-9999

Krummel, P. B., Langenfelds, R. L., & Loh, Z. (2021q). Atmospheric H2 at South Pole by Commonwealth Scientific and Industrial Research Organisation, dataset published as H2_SPO_surface-flask_CSIRO_data1 at WDCGG, ver. 2021-07-05-0440. https://doi.org/https://doi.org/10.50849/WDCGG{_}0016-7011-4001-01-02-9999

Krummel, P. B., Langenfelds, R. L., & Loh, Z. (2021r). Atmospheric H2 by Aircraft (over Bass Strait and Cape Grim), Commonwealth Scientific and Industrial Research Organisation, dataset published as H2_AIA_aircraft-flask_CSIRO_data1 at WDCGG, ver. 2021-07-05-0440. https://doi.org/https://doi.org/10.50849/WDCGG{_}0016-8003-4001-05-02-9999

Paulot, F., Paynter, D., Naik, V., Malyshev, S., Menzel, R., & Horowitz, L. W. (2021). Global modeling of hydrogen using GFDL-AM4.1: Sensitivity of soil removal and radiative forcing. *International Journal of Hydrogen Energy*, *46*(24), 13446–13460. https://doi.org/10.1016/j.ijhydene.2021.01.088

Table S1: List of aldehydes in the MCM, along with photolysis products and rates (J [s^{-1}]) for the H_2 channel estimated with 1%, 2%, 5% and 10% quantum yields applied across wavelengths.

Aldehyde	**MCM ID**	**Photolysis products**[a]	**JID**	J **1% qy**	J **2% qy**	J **5% qy**	J **10% qy**
Formaldehyde (Methanal)	HCHO[b]	H2 + CO	J12	-	-	-	-
Glyoxal (oxaldehyde)	GLYOX[b]	CO + CO + H2	J31	-	-	-	-
Acetaldehyde	CH3CHO	CH2CO[c] + H2	J62	4.37E-07	8.74E-07	2.18E-06	4.37E-06
Propanal	C2H5CHO	C2H4 + H2 + CO	J63	5.68E-07	1.14E-06	2.84E-06	5.68E-06
Butanal	C3H7CHO	C3H6 + H2 + CO	J64	6.76E-07	1.35E-06	3.38E-06	6.76E-06
Isobutylaldehyde	IPRCHO	C3H6 + H2 + CO	J65	5.49E-07	1.10E-06	2.74E-06	5.49E-06
Acrolein (2-propenal)	ACR	C2H2 + H2 + CO	J66	2.44E-06	4.89E-06	1.22E-05	2.44E-05
(2-methylprop-2-enal)	MACR	C3H4 + H2 + CO	J67	3.05E-07	6.09E-07	1.52E-06	3.05E-06
Methylglyoxal (2-oxopropanal)	MGLYOX	CH2CO[c] + H2 + CO	J68	4.42E-07	8.83E-07	2.21E-06	4.42E-06
HPALD (2-hydroperoxyacetaldehyde)	HCOCH2OOH	H2 + Other products	J69	4.65E-08	9.30E-08	2.32E-07	4.65E-07
Glycolaldehyde (2-hydroxyacetaldehyde)	HOCH2CHO	HCHO + H2 + CO	J70	1.07E-07	2.15E-07	5.37E-07	1.07E-06
3-Hydroxy 2-Methylpropanal	HOIPRCHO	H2 + Other products	J71[d]	6.76E-07	1.10E-06	3.38E-06	6.76E-06
Lactaldehyde	CH3CHOHCHO	H2 + Other products	J71[d]	6.76E-07	1.10E-06	3.38E-06	6.76E-06
3-Oxopentanal	CO3C4CHO	H2 + Other products	J71[d]	6.76E-07	1.10E-06	3.38E-06	6.76E-06
3-Hydroxy-pentanal	HO3C4CHO	H2 + Other products	J71[d]	6.76E-07	1.10E-06	3.38E-06	6.76E-06
3-Hydroxypropanal	HOC2H4CHO	H2 + Other products	J71[d]	6.76E-07	1.10E-06	3.38E-06	6.76E-06
2-Hydroxybutanal	HO3C3CHO	H2 + Other products	J71[d]	6.76E-07	1.10E-06	3.38E-06	6.76E-06
4-Hydroxybutanal	HOC3H6CHO	H2 + Other products	J71[d]	6.76E-07	1.10E-06	3.38E-06	6.76E-06

[a] Expressed with the identification used in the MCM.
[b] Species in MCM that already include the photolytic generation of H_2. The photolysis rates were kept the same for all tests.
[c] The ketene CH_2CO generated in the photolysis channel was replaced with glycolaldehyde as described in the text.
[d] In absence of aldehyde-specific cross section measurements, the photolysis rate of butanal was used as a surrogate in each case.
Names in parenthesis are IUPAC names

Table S2: Calculated metrics at each measuring site from the Krummel et al., 2021j, 2021k, 2021l, 2021m, 2021n, 2021o, 2021p, 2021q dataset

Site ID	Site name	Lat	Lon	Hemisphere	Lat. band	Gas	Start[a]	End[b]	N. obs[c]	Mean Mod. [ppb]	Mean Obs. [ppb]	r	RMSE	MB	NMB	MFB	NME	FE	FB
ALT	Alert	82.4991	-62.3415	NH	HNH	H2	2015-01	2016-12	24	494.86	489.93	0.93	9.30	4.93	1.01	0.01	1.62	1.63	1.00
MHD	Mace Head	53.33	-9.9	NH	HNH	H2	2015-01	2016-12	24	502.40	515.91	0.95	15.99	-13.51	-2.62	-0.03	2.62	2.70	-2.70
MLO	Mauna Loa	19.5362	-155.5762	NH	LNH	H2	2015-01	2016-12	24	530.12	536.51	0.54	11.53	-6.39	-1.19	-0.01	1.60	1.62	-1.21
CFA	Cape Ferguson	-19.2773	147.0584	SH	LSH	H2	2015-01	2016-12	20	483.79	546.30	0.52	60.87	-60.26	-11.03	-0.10	11.03	9.74	-9.74
CGO	Cape Grim	-40.6822	144.6883	SH	LSH	H2	2015-01	2016-12	24	508.42	547.37	0.74	39.44	-38.95	-7.12	-0.07	7.12	7.39	-7.39
MQA	Macquarie Island	-54.4985	158.9385	SH	HSH	H2	2015-01	2016-12	24	513.94	547.78	0.84	34.04	-33.84	-6.18	-0.06	6.18	6.38	-6.38
CYA	Casey	-66.2833	110.5167	SH	HSH	H2	2015-01	2016-12	24	516.11	546.93	0.87	30.98	-30.82	-5.64	-0.06	5.64	5.80	-5.80
MAA	Mawson	-67.6047	62.8706	SH	HSH	H2	2015-01	2016-12	14	516.20	551.72	0.54	34.05	-33.90	-6.14	-0.04	6.14	3.70	-3.70
SPO	South Pole	-89.9969	-24.8	SH	HSH	H2	2015-01	2016-12	24	516.12	547.13	0.87	31.16	-31.01	-5.67	-0.06	5.67	5.83	-5.83

[a]Corresponds to the first date available in the measurements from Krummel et al., (2021a-i) used in the calculation of metrics.

[b]Corresponds to the last date available in the measurements from Krummel et al., (2021a-i) used in the calculation of metrics.

[c]Number of measurements used to compare during the period covered by the start [a] and end [b] dates.